Nanoparticles on surfaces: resonances and optical forces

J. Ricardo Arias Gonzales, Patrick C. Chaumet, and M. Nieto-Vesperinas

Instituto de Ciencia de Materiales de Madrid Consejo Superior de Investigaciones Científicas, Campus de Cantoblanco, 28049 Madrid. Spain

1. – Introduction

2. – Resonances

2˙1. *Introduction.* – There is an increasing interest in the study of electromagnetic eigenmodes of small particles. On the one hand, experiments on the linewidth of surface plasmons in metallic particles [1] and on the evolution of their near fields, both in isolated particles and in arrays, [2] aim to a basic research and possible applications of their optical properties. On the other hand, experimental works of Mie resonance excitation and whispering-gallery modes [3, 4, 5, 6, 7] put forward a possible interest of these systems for their use as field concentrators and high-Q cavity devices. Also, in near field optical studies [8, 9], small particles can act either as detectors or emitters [10, 11, 12, 13], thus their resonant behavior will greatly enhance their usefulness. In addition, the analogy of eigenmodes with electron orbitals, suggest the possibility to form bonding and antibonding interactions between neighbouring particles [14] and thus to introduce, through light action, attractive interactions this leading to ensambling them in desired nanostructures through optical binding. [15, 16]

Electromagnetic resonances in objects can be classified into two groups:

- Morphology-dependent resonances, *MDR*, or Whispering Gallery Modes, *WGM*. They appear at non metallic particles and are strongly dependent on the object's morphology, internal structure (optical contrast in the dielectric permittivity between the particle and the surrounding medium), and the size and frequency of

the incident light (through the so called *Size parameter*: $x = 2\pi a/\lambda$, a being the particle radius).

- Surface plasmon resonances, *SPR*. When they are excited, they produce electromagnetic propagation of electron oscillations in metallic surfaces such as the ones of small particles.

Both of them are associated with surface waves with exponential decay out from the particle surface.

The existence of resonances must be taken into account at a wide variety of phenomena. High field enhancements are produced close to the particle surface altering any surface spectroscopy. Nonlinear effects can be found at Fluorence emission, Spontaneous Raman emission, Stimulated Raman scattering, Stimulated Brillouin scattering, Coherent Anti-Stokes Raman scattering and Coherent Raman mixing, Bistability and so on. The excitation of resonances can produce lasing (they behave as small resonators), and can generate second harmonic.

They have been widely applied up to now. Some examples are:

- Measurements of evaporation rate, temperature, surface tension and viscosity. The shift of resonance's position of known particles becomes a method for this kind of measurements.
- Measurements of droplet shape deformation. The splitting of resonances account for the deviation from an initial particle shape.
- Characterization of Sprays.
- Fluorescence and Spontaneous Raman emission.

Morphology-dependent resonances are interpreted as rays or beams propagating around the object, confined by an almost total internal reflection, returning to the starting point in phase. A *Quality factor* is also defined as $Q = 2\pi$ (Stored energy) / (Energy lost per cycle) $= \omega_0/\delta\omega$, where ω_0 is the resonace frequency and $\delta\omega$ the resonance full width. The first theoretical studies of *MDR* were performed by Gustav Mie, whose *Mie theory* in spheres has largely extended. The scattered field, either outside or within the particle, is decomposed into a sum of partial waves. Each partial wave is weighed by a coefficient whose poles explain the existence of peaks at the scattering cross section. These poles correspond to complex frequencies but true resonances (real values with non infinity height for the peaks) have a size parameter value close to the real part of the complex poles. The imaginary part of the complex frequency accounts for the width of the resonance peak. The *MDR* are classified by three integer numbers: one related with the partial wave (*order number*), another one which accounts for the several poles which can present the same coefficient (*mode number*), and a third one accounting for the degeneration of a resonance (*azimuthal mode number*). In the first experimental check at optical frequencies, [17] the variation of the radiation pressure (due to *MDR*) on highly transparent, low-vapor-pressure silicone oil drops (index $1.4 - 1.53$) was measured. The

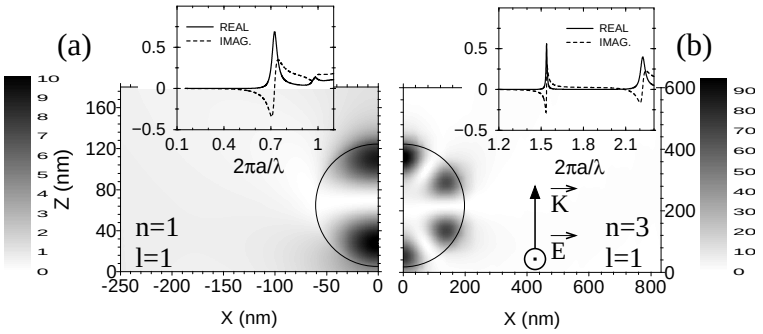

Fig. 1. – Plots of $|E/E_o|^2$ for an isolated silicon sphere illuminated by a plane incident wave, as shown by the picture inside 1(b). 1(a): $a = 60$ nm and $\lambda = 521$ nm. 1(b): $a = 200$ nm and $\lambda = 817$ nm. Insets: real (solid line) and imaginary (dashed lines) parts of the (n, l) external Mie coefficient amplitude of the TE mode.

drops were levitated by optical techniques and the incident beam was focused at either the edge or the axis of the particles showing the creeping nature of the surface waves.

It is important, when speaking about resonances, to mention the *Glory* effects [18, 19, 20] that have been found in water droplets. The *Glory theory* accounts for the backscattering intensity enhancements found in water droplets. These enhancements are associated with rays grazing the surface of the droplet, involving hundreds of circumvolutions (surface effects). Axial rays (geometrical effects) also contribute. They have been observed in large particle sizes ($x > 10^2$) and no glory effects have been found for sizes in the range $x \sim 1$. These backscattering intensity enhancements cannot be associated to a unique partial wave, but a superposition of several partial waves. Whenever a resonance is matched in a large particle, Glory effects take places but it is not truth the inverse assertion.

2˙2. *Near and Far field resonant scattering.* – The near field outside and within the particles [22] show a charasteristic lobe pattern depending on the resonance excited. In fig. 1 is shown the resonant near field distributions $|E/E_o|^2$ (E_o being the electric incident field) for propagating plane wave excitation on an isolated silicon sphere with either $a = 60$ nm (fig. 1(a)) or $a = 200$ nm (fig. 1(b)). These are shown in a plane containing the sphere equator, parallel to the incident wavevector and perpendicular to the incident electric vector. The resonance's position in wavelengths are $\lambda = 521$ nm with $n = (4.195, 0.058)$, and $\lambda = 817$ nm with $n = (3.677, 0.005)$. The modes are identified [23] (by the numbers explained above) as TE with $n = 1$, $l = 1$ for $a = 60$ nm, and $n = 3$, $l = 1$ for $a = 200$ nm. The latter are rather similar to the whispering-gallery modes studied in larger particles (cf. refs. [4, 5, 6, 7]). The insets show the charasteristic behavior of the external Mie coefficient amplitude whenever a resonance is matched.

The peak positions and widths of the resonances are not perturbed by the kind of incidence, but the peak heights depends on the excitation. [22, 24] Figure 2 shows the

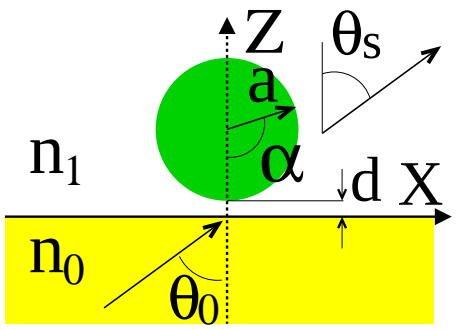

Fig. 2. – Scattering geometry

scattering geometry for a particle on a dielectric surface. Figure 3 shows the scattering efficiencies for an isolated silicon cylinder in vacuum with size $a = 200$ nm. The incident field is either propagating or evanescent, created with $\theta_o = 60^o$. The interaction with the plane at which the evanescent wave has been created has not been taken into account. The polarization of the incident wave is S-polarized (electric field parallel to the cylinder axis), fig. 3(a), or P-polarized (magnetic field parallel to the cylinder axis), fig. 3(b). When the incident wave is evanescent, the intensity is normalized to the incident intensity averaged over the cross-sectional area of the sample perpendicular to the incident Poynting vector. Namely, to:

$$\tilde{I}_0 = \frac{1}{2a}\int \langle \mathbf{S_{inc}} \rangle \, \mathbf{n} dA = I_0 \frac{n_0}{n_1} \sin\theta_0 \exp(-2\kappa d) \frac{\sinh(2\kappa a)}{2\kappa a} \tag{1}$$

where n_0 and n_1 are the refractive indices of air and the surface on which the particle is located, respectively, $\kappa = 2\pi/\lambda(n_0^2 \sin^2\theta_0 - n_1^2)^{1/2}$ and I_0 represents the incident intensity. The peak height strongly depends on the excitation, being larger for evanescent waves. This efficiency difference is more important as the size of the cylinder increases.

2˙3. *Presence of a surface.* – A procedure that permits predicting and controlling the eigenmode excitation should be put forward. This requires to include in the model the presence of interfaces [24, 25] that act as light couplers between the particle and the illuminating wavefield. Near field measurements must account of the resonances. Nanometer particle response at optical wavelengths must be studied for the development of nanotechnology: *Optical binding*, *nanodetection* and *nanoemission* (new possibilities of resolution and local emission), *Optical Force Microscopy* and so on.

Figure 4 shows the scattered efficiencies (normalized as eq. (1)) at fixed scattering angles versus wavelength for two silver cylinders of radius: $a = 30$ nm, fig. 4(a), and $a = 200$ nm, fig. 4(b). Incident plane waves, either propagating or evanescent, are considered for the cases of isolated cylinders, and Gaussian beams when the interaction

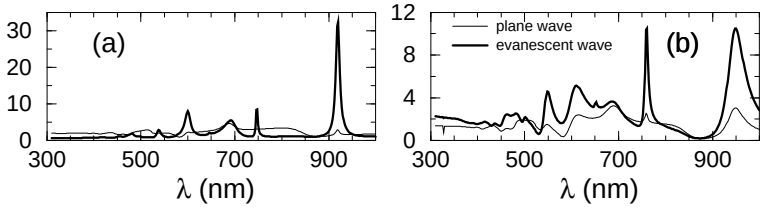

Fig. 3. – Scattering Efficiency for an isolated silicon cylinder of radius $a = 200$ nm. The incidence is done with a plane wave either propagating or evanescent (see the code). 3(a): S polarization. 3(b): P polarization.

with the plane is taken into account (P polarization). The distance d from the bottom of the object to the plane is considered either 15.5 nm for an incident evanescent plane wave in the presence of the plane, or zero for the rest of the cases. The enhancement observed is due to the plasmon resonance excited under P polarization. For S polarization, no plasmon resonance is excited in a cylinder, though it is allowed in a non-cylindrical object like a sphere, since this geometry depolarizes the incident wave. The curves for the isolated particle keep remarkable similarity with the corresponding scattering efficiencies thus showing the contribution of large angle differential cross sections to the resulting efficiency. Although not shown here for the sake of brevity, however, the intensity can be larger for incident propagating waves than for incident evanescent waves at scattering angles close to the forward direction of the propagating wave.

Adding the multiple scattering due to the presence of the plane (see the code), we

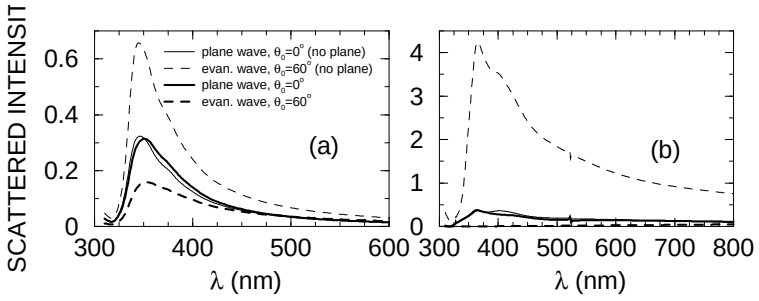

Fig. 4. – Normalized scattered intensity at $\theta_s = 45^o$ versus wavelength for a silver cylinder of radius either $a = 30$ nm, 4(a) or $a = 200$ nm, 4(b). The cylinder is placed at $d = 0$ for the isolated cases and at $d = 15.5$ nm when it is placed on a dielectric plane with length either $L = 30500$ nm, 4(a), or $L = 40500$ nm, 4(b). The incidence is a P polarized plane wave, either propagating or evanescent, when the particle is isolated, and a Gaussian beam with $HWHM$ either $W = 3050$ nm, 4(a), or $W = 4050$ nm, 4(b), when the interaction with the plane is taken into account.

observe the decrease, broadening and red-shift of the peak. For evanescent wave excitation, this peak decrease is remarkable, since the lineshape is lower than that from the incident plane wave. In this case, to the above explanation we have to add that multiple scattering at the surface breaks the nearly isotropic radiation obtained in the absence of interaction, leading to a rather directional scattered intensity into the glass medium [26]. In this way the intensity at scattering angles not very close to this main direction is largely reduced. This effect is amplified for larger object sizes, as shown in fig. 4(b). These results are similar when considering Morphology-dependent resonances.

Figure 5 shows the normalized near field intensity spatial distribution ($|H/H_o|^2$, H_o being the incident magnetic field) for a silicon cylinder with radius $a = 60$ nm on the dielectric plane at distance $d = 5$ nm for P polarization at the resonant wavelengths: $\lambda = 471$ nm [$n = (4.485, 0.101)$], figs. 5(a) and 5(c), and $\lambda = 638$ nm [$n = (3.872, 0.018)$], figs. 5(b) and 5(d) respectively. The length of the plane dielectric surface in the computation is $L = 34000$ nm, $W = 4000$ nm. Large field concentrations are obtained for P polarization. However, for S polarization the field distribution spreads outside the cylinder with a no so high enhancement inside (not shown here for the sake of brevity). This behavior of the near field distribution remains at both wavelengths: P polarization concentrates almost all the incident field inside the cylinder leading to low eigenmodes. On the other hand, evanescent incident wave excitation (created under TIR) shifts this distribution to that of the coupling with the surface wave refracted under TIR, i.e. it rotates this near field intensity distribution by 90^o, and slightly displaces it towards the flat surface. Notice that the lower values of this intensity are due to the decay of the evanescent wave at the cylinder. At the same time, evanescent wave excitation is more effective for field concentration, since the ratio of the intensity field distribution to that of the incident intensity along the plane $z = d + a$, is larger in this case. The number of lobes must be $2n$ along the perimeter. The average field intensity integrated on a circle, centered at the cylinder axis, as a function of the radius of the particle, must show l lobes. Thus, the corresponding Mie coefficient [21] for figs. 5(a) and 5(c) are $n = 1$ and $l = 1$, and for figs. 5(b) and 5(d), $n = 0$ and $l = 1$. The insets in figs. 5(c) and 5(d) show the amplitude of the external Mie coefficient for these resonances. For such small cylinder sizes, multiple scattering effects between the flat surface and the cylinder are not very large.

Figure 6 shows the intensity distribution $|E/E_0|^2$ for the S wave resonance at $\lambda = 919$ nm (index $n = (3.670, 0.005)$). In figs. 6(a) and 6(c) is plotted the normalized intensity when the particle is isolated and the incident wave is plane either propagating or evanescent, respectively. Figures 6(b) and 6(d) show the field distribution in the presence of the surface after multiple scattering at the flat interface has been taken into account ($L = 40000$ nm). The incident wave is a Gaussian beam with $W = 4000$ nm at either $\theta_0 = 0^o$ or $\theta_0 = 60^o$, respectively. The distance is $d = 15$ nm. This resonant structure has large near field concentrations taking place inside the particle. For plane propagating wave illumination we can explain the resulting lobe pattern as an interference between counterpropagating evanescent surface waves. The damping is very important for this particle size and the multiple scattering between particle and plane acts by smearing the contrast. The slighter lobe pattern in figs. 6(c) and 6(d), corresponding to evanescent

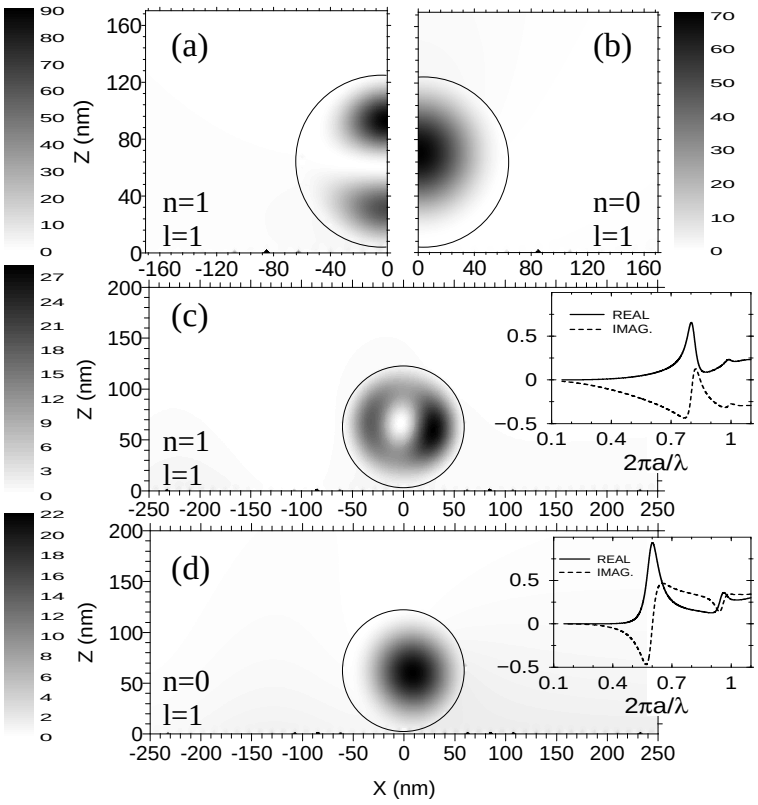

Fig. 5. – Plots of $|H/H_o|^2$ for P polarization for a cylinder with $a = 60$ nm on a plane at $d = 5$ nm and $W = 4000$ nm. 5(a): $\lambda = 471$ nm, $\theta_o = 0^o$. 5(b): $\lambda = 638$ nm, $\theta_o = 0^o$. 5(c): $\lambda = 471$ nm, $\theta_o = 60^o$. 5(d): $\lambda = 638$ nm, $\theta_o = 60^o$. The circular lines show the boundary of the cylinder. Insets: real (solid line) and imaginary (dashed line) parts of the (n, l) external Mie coefficient amplitude.

wave illumination of the particle, either isolated or in presence of the plane, is attributed to the conversion of evanescent waves on the plane to surface waves in the particle. This is seen in the inset of fig. 6(c), which shows the field $|E/E_0|^2$ along a concentrical line for the cylinder either isolated (thin lines) or on the plane (thick lines). Solid lines correspond to propagating plane wave illumination at $\theta_0 = 0^o$ and dashed lines, show results for illumination with an evanescent wave at $\theta_0 = 60^o$. The other parameters are the same as before. The lobe pattern has a higher contrast when the object is isolated. The incident propagating plane wave also contributes to enhance this contrast. Then, the more propagating the incident waves is, the higher the contrast for the modes of a resonance become because of the resulting counterpropagating surface wave interference. This resonance in fig. 6 is identified as that with $n = 3$, $l = 1$. The corresponding Mie coefficient is shown in the inset in fig. 6(d). The real and imaginary parts of this

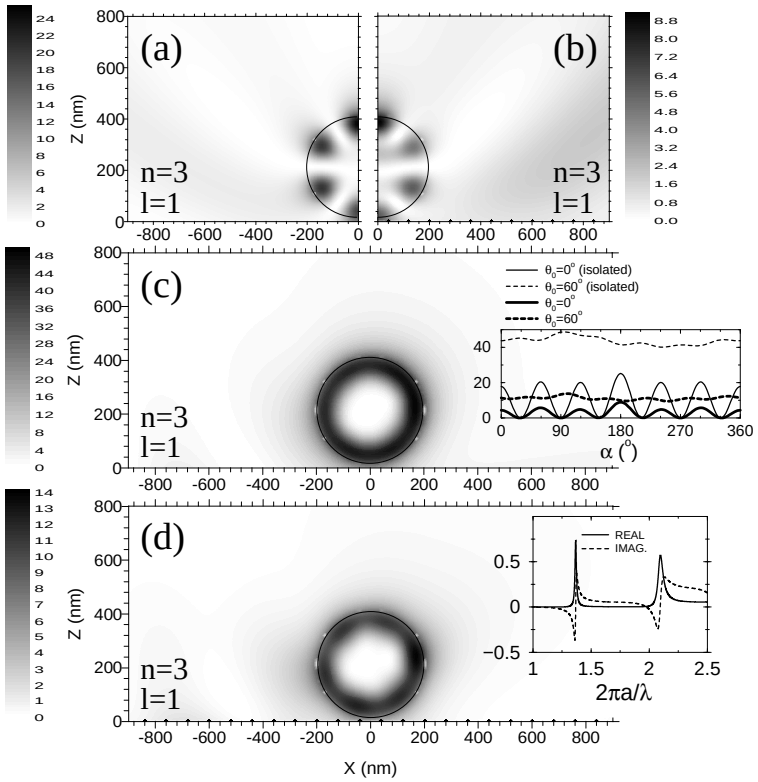

Fig. 6. – $|E/E_o|^2$ for S polarization for a silicon cylinder with $a = 200$ nm and $\lambda = 919$ nm. 6(a): isolated object illuminated by a plane propagating wave at $\theta_o = 0^o$. 6(b): Object on a dielectric plane at $d = 15$ nm and $L = 40000$ nm, illuminated by a Gaussian beam ($W = 4000$ nm) at $\theta_o = 0^o$. 6(c): isolated object illuminated by an evanescent plane wave at $\theta_o = 60^o$ ($d = 15$ nm). 6(d): Object on a plane at $d = 15$ nm and $L = 40000$ nm, illuminated by a Gaussian beam ($W = 4000$ nm) at $\theta_o = 60^o$. The circular lines show the boundary of the cylinder. Inset 6(c): normalized near field intensity along an internal circumference of radius $r = 165$ nm; solid and dashed thin lines: isolated cylinder excited by either a plane propagating wave ($\theta_o = 0^o$) or a plane evanescent wave ($\theta_o = 60^o$), respectively. Solid and dashed thick lines: cylinder on a plane excited by a Gaussian incident beam of $W = 4000$ nm at either $\theta_o = 0^o$ or $\theta_o = 60^o$, respectively. Inset 6(d): real (solid line) and imaginary (dashed line) parts of the (n, l) external Mie coefficient amplitude.

coefficient have the characteristic jump at the resonant wavelength.

The near field intensity distributions for metallic particles is different. Next, silver cylinders are analysed. Figure 7 shows the intensity near field $|H/H_0|^2$ for an incident P wave either at $\theta_0 = 0^o$ (figs. 7(a) and 7(b)) or $\theta_0 = 60^o$ (figs. 7(c) and 7(d)), at which total internal reflection (TIR) occurs in absence of the object, for a silver cylinder with $a = 30$ nm. Figures. 7(a) and 7(c) correspond to off-resonance (incident wavelength:

$\lambda = 317$ nm, refractive index $n = (0.978, 0.509)$) and figs. 7(b) and 7(d) to on-resonance (incident wavelength: $\lambda = 346$ nm, refractive index $n = (0.234, 1.275)$). The distance from the plane to the bottom of the cylinder is fixed at $d = 5$ nm, $L = 30500$ nm and $W = 4000$ nm. In this latter figure at $\theta_0 = 0^o$, we observe an intensity enhancement on-resonance almost four times higher than off-resonance at plane wave excitation (fig. 7(b)). Such enhancement is localized just at the space between the cylinder and the flat dielectric surface and corresponds to a field distribution more concentrated than off-resonance. In case of evanescent wave excitation, a lower enhancement at resonance is observed (fig. 7(d)) but it has a higher field concentration below the cylinder than off-resonance, (fig. 7(c)), where the maximum intentity spreads along the flat dielectric surface. It is also worth noticing how this field concentration on-resonance by the particle (fig. 7(d)) is in contrast with the transmitted field distribution off-resonance (fig. 7(c)) that mainly corresponds to the evanescent surface wave created under TIR.

Figure 8 shows intensity near field distributions $|H/H_0|^2$ for a larger particle, its radius is now $a = 200$ nm. We again consider multiple scattering of light with the flat interface and P polarization. Figures 8(a) and 8(c) show a case off-resonance at either $\theta_0 = 0^o$ or $\theta_0 = 60^o$, respectively (incident wavelength: $\lambda = 317$ nm, index $n = (0.978, 0.509)$). The distance from the plane to the bottom of the cylinder is $d = 15$ nm, $L = 30000$ nm and $W = 4000$ nm. Now the field cannot deeply penetrate inside the cylinder and thus the intensity is primarily concentrated on its surface, close to the flat interface. Off-resonance, the intensity maximum is similar to those previously obtained for smaller sizes. However, the spatial intensity distribution is more inhomogeneus since now the particle is big enough to highly scatter and distort the field, thus higher multipolar orders of the electromagnetic field playing a more relevant role. Qualitatively, those characteristics previously described for the smaller size, are enhanced in this case of larger particles. The shadow contrast at both sides of the particle for an incident plane wave, is larger. At on-resonance excitation (incident wavelength: $\lambda = 366$ nm, index $n = (0.186, 1.621)$), figs. 8(b) and 8(d), there is an enhancement of the intensity very close to the particle surface, as expected, due to the plasmon travelling along the particle surface. The diffraction fringes outside the particle at plane wave excitation have high contrast (fig. 8(b)) whereas at evanescent wave excitation, the particle swallows the field and concentrates it at the bottom of its surface (fig. 8(d)), (compare with the off-resonance case which shows the distribution concentrated at the surface wave travelling along the flat interface (fig. 8(c)). However, the enhancement is now higher for evanescent wave incidence. This is explained as due to the better excitation of higher multipolar orders of the field by inhomogeneus waves contributing to enhance the plasmon resonance.

A regular fringe pattern is also observed on the top hemisphere of the particle (plane wave excitation) very similar to the lobe pattern observed for high index dielectric particles [22] with the same radius (as previously). We can explain this as an interference between counterpropagating surface plasmon waves. This radiates outside with a corresponding fringe pattern.

The multiple scattering at the flat interface acts mainly diminishing and broadening the peak intensity. The red-shift produced is known of a few nanometers, but given

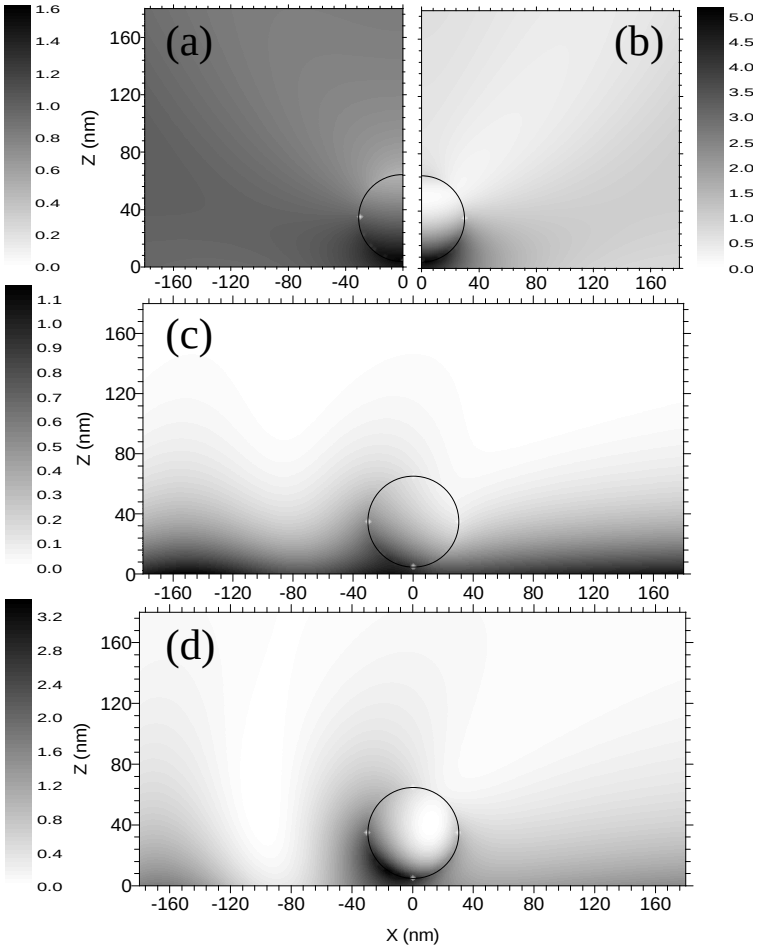

Fig. 7. – $|H/H_o|^2$ for P polarization for a silver cylinder with $a = 30$ nm on a dielectric plane at $d = 5$ nm; $L = 30500$ nm and $W = 4000$ nm. 2(a): $\lambda = 317$ nm, $\theta_o = 0^o$. 2(b): $\lambda = 346$ nm, $\theta_o = 0^o$. 2(c): $\lambda = 317$ nm, $\theta_o = 60^o$. 2(d): $\lambda = 346$ nm, $\theta_o = 60^o$. The circular lines show the boundary of the cylinder.

the lineshape width, it is relatively small with such a transparent interface. [22] The resonances, however have a width large enough to obscure this red-shift effect. The peak decrease is estimated as 13% (from 3.7 to 3.2) for the plane wave case, and as 32% (from 7.1 to 4.8) for the evanescent wave case ($a = 200$ nm).

2˙4. *Conclusions*. – A detailed study of eigenmode excitation in both metallic and dielectric nanoparticles on a flat dielectric surface is presented. Multiple scattering between the particle and the surface has been taken into account. We have analysed the

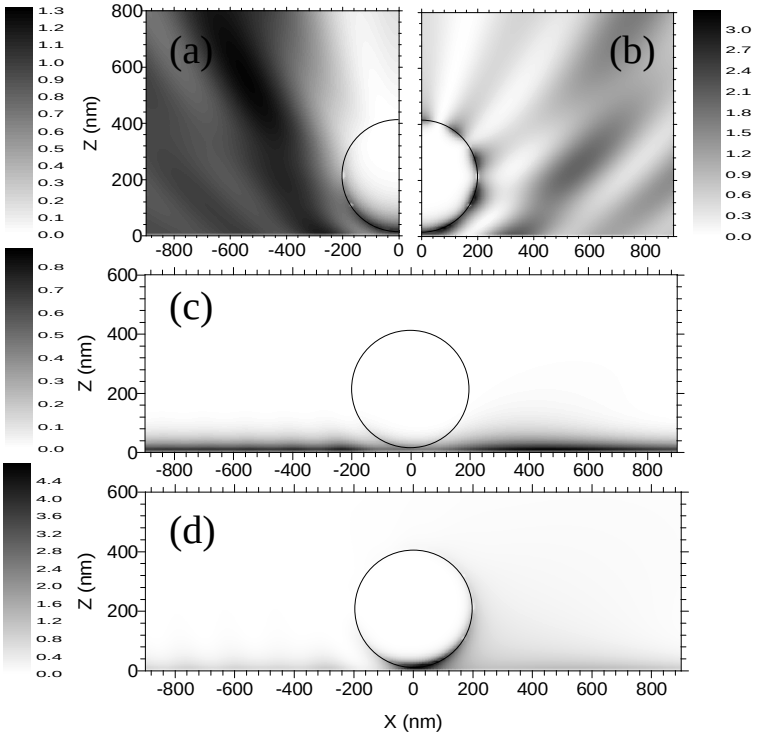

Fig. 8. – $|H/H_o|^2$ for P polarization for a silver cylinder with $a = 200$ nm on a dielectric plane at $d = 15$ nm; $L = 30000$ nm and $W = 4000$ nm. 2(a): $\lambda = 317$ nm, $\theta_o = 0^o$. 2(b): $\lambda = 366$ nm, $\theta_o = 0^o$. 2(c): $\lambda = 317$ nm, $\theta_o = 60^o$. 2(d): $\lambda = 366$ nm, $\theta_o = 60^o$. The circular lines show the boundary of the cylinder.

effects of this interaction on both near and far field scattered intensity distributions. The incidence takes place from the dielectric side, either normally to the surface plane, or under total internal reflection thus creating a transmitted evanescent wave which circulates at the flat interface and excites the particle eigenmodes.

In the far zone, the scattering efficiency shows sharp peaks, associated to the excitation of either plasmon resonances (in metallic particles) or Morphology-dependent resonances (in dielectric particles), which are further enhanced on incidence with an evanescent plane wave. At discrete scattering angles well separated from the forward direction, the scattered intensity keeps very close to this behavior of the scattering efficiencies. When multiple interaction with the interface is taken into account, it is that lineshape due to evanescent plane wave excitation which keeps below the one from incident propagating plane waves. This is more noticeable as the size of the object increases.

In the near field, the stucture of both kind of resonances is observed: we obtain plasmon resonances whose wave field is located very close to the particle surface, with

its maximum of intensity being reached outside. For dielectric particles, however, the intensity maximum of the Mie resonant modes is located inside the particle. Special care must be taken with the polarization for dielectric particles: P polarized incidence shows higher field concentration inside the particle with intensity maxima larger than with S polarization. An interference pattern is created within the particle surface for both kind of resonances when incident propagating plane wave takes place. The interaction with the flat interface slightly breaks the mode structure and diminishes the peak intensity in both cases. The incidence with an evanescent wave acts by smearing the contrast of the mode pattern in dielectric particles, and by concentrating the intensity at the bottom side of the particle in metallic particles, due to the higher absortion of the latter. Besides, in dielectric particles, the pattern rotates with the angle of incidence of the exciting wave. An interference between the incident evanescent wave and the reflected wave at the incidence wave side of the particle is also observed.

3. – Optical forces

3˙1. *Introduction.* – This part deals with the optical forces. It has been shown by Ashkin and coworkers [27, 28] the possibility to act mechanically upon small particles with radiation pressure. A consequence of these works was the invention of the optical tweezer for non destructive manipulation of suspended particles [29] or molecules and other biological objects [30, 31, 32]. Recently, these studies have been extended to the nanometer scale [33, 34, 35, 36, 37, 38], and multiple particle configurations based on optical binding have been studied [15, 39, 40, 14, 41]. The effect of evanescent waves created by total internal reflection on a dielectric surface upon particles has also been studied, experimentally in Ref. [42], and theoretically in Refs. [43, 44]. In Ref. [43] no multiple interaction of the light between the particles and the dielectric surface was taken into account. On the other hand, in Ref. [44] a multiple scattering numerical method was put forward limited to a 2-D configuration.

It is worth remarking here that several previous theoretical works on optical forces usually employ approximations depending on the radius of the particle; if the particle is small it has been usual to split the force into three parts: the gradient, scattering, and absorbing forces [45]. However, when the radius of the particle grows, or if the shape of the particle is not spherical, or in the case of an evanescent wave illuminating the sphere, it is not possible to use this method. Hence, we will use a rigorous and exact calculation by using the Maxwell's stress tensor. [46] Some work has been done with this approach in free space [33, 47], or for a spherical particle over a dielectric surface illuminated by a Gaussian beam. [48]

3˙2. *Theory.* –

3˙2.1. The Maxwell's stress tensor. The force on an object due to the electromagnetic field can be computed from Maxwell's stress tensor. [46] At optical frequencies involved in many experiments, however, only the time average of the electromagnetic force is

observed, hence the time averaged force is :

$$\mathbf{F} = 1/(8\pi)\Re e\Big[\int_S \big[(\mathbf{E}(\mathbf{r},\omega).\mathbf{n})\mathbf{E}^*(\mathbf{r},\omega) + (\mathbf{H}(\mathbf{r},\omega).\mathbf{n})\mathbf{H}^*(\mathbf{r},\omega) - 1/2(|\mathbf{E}(\mathbf{r},\omega)|^2 + |\mathbf{H}(\mathbf{r},\omega)|^2)\mathbf{n}\big]d\mathbf{r}\Big], \tag{2}$$

where S is a surface enclosing the object, $\mathbf{n}$ is the local outward unit normal, $*$ denotes the complex conjugate, and $\Re e$ represents the real part of a complex number. Let us notice that Eq. (2) is written in CGS units for an object in vacuum. Notice than an other form of the Maxwell's stress tensor exist :

$$\mathbf{F} = 1/(8\pi)\Re e\Big[\int_V \big[\rho(\mathbf{r},\omega)\mathbf{E}^*(\mathbf{r},\omega) + \mathbf{J}(\mathbf{r},\omega)\times\mathbf{B}^*(\mathbf{r},\omega)\big]d\mathbf{r}\Big], \tag{3}$$

with $\rho(\mathbf{r},\omega)$ the polarization charge density, $\mathbf{J}(\mathbf{r},\omega)$ the polarization current density and V the volume of integration. This second form is more easy to read physically: the first and second term represents the resultant forces acting, respectively, on the charge and the current.

3˙2.2. The coupled dipole method used for compute the optical forces. For compute the optical forces, through the Maxwell's stress tensor, we use the coupled dipole method (CDM). The CDM was introduced by Purcell and Pennypacker in 1973 for studying the scattering of light by non-spherical dielectric grains in free space.[49] The object under studied is represented by a cubic array of N polarizable subunits. Each subunit gets a dipole moment, due to the incident field, and the field radiated by the other subunits. Then the field radiated by the object at the position $\mathbf{r}$ is the sum of the incident field and the field radiated by the N subunits. In presence of a flat dielectric surface the procedure is the same but we must take into account of the interaction between the subunits and the surface. [50]

For compute the optical forces we use Eq. (3) of the Maxwell's stress tensor. As the subunits are small Eq. (3) can rewritten with the help of the dipole moment of the subunit and the value of the field at its position: [51, 52]

$$F_k(\mathbf{r}_i) = (1/2)\Re e\left(p_{il}(\mathbf{r}_i,\omega)\left(\frac{\partial}{\partial k}E^l(\mathbf{r},\omega)\right)^*_{\mathbf{r}=\mathbf{r}_i}\right), \tag{4}$$

where k and l stand for the components along either x, y or z. Hence, we use Eq. (4), for get the force at each subunit of the discretization, and the total force is only their sum. Notice that if the sphere under studied is small in compare to the wavelength we can do the dipole approximation and use directly Eq. (4) without the process of discretization of the CDM.

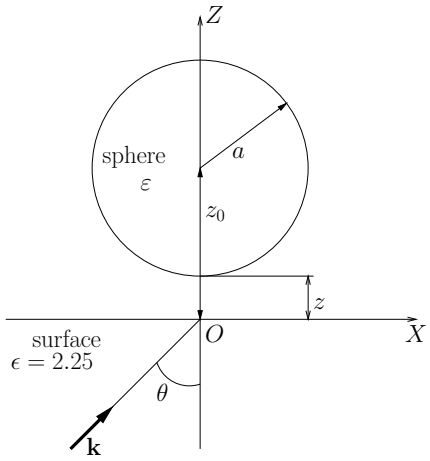

Fig. 9. – Geometry of the configuration considered. Sphere of radius a on a dielectric flat surface ($\epsilon = 2.25$). The incident wave vector $\mathbf{k}$ is in the XZ plane.

3˙3. *Results and discussions.* – The situation under study is represented by fig. 9. We will compute the optical forces with different radius a and at different angle of incidence and distance sphere-surface.

3˙3.1. Force on a small sphere.

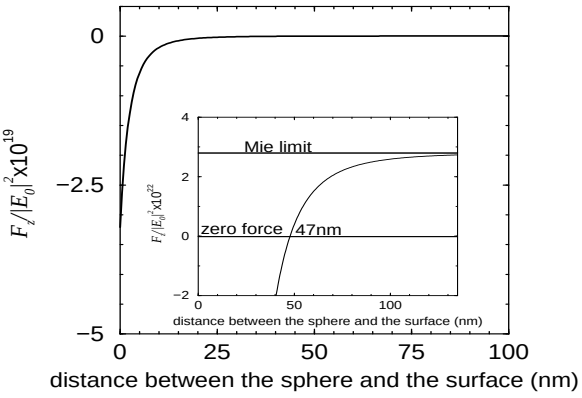

Fig. 10. – Normalized force in the Z-direction for a sphere of radius $a = 10$nm. The incidence angle is $\theta = 0°$. The inset shows the force after $z = 50$nm. The first horizantal line is the zero force and the second line the Mie limit.

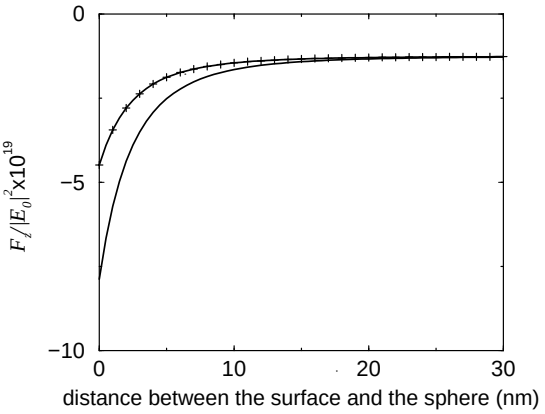

Fig. 11. – Normalized force in the Z direction for the sphere with an incidence angle largest than the critical angle: $\theta = 42°$. Curve without symbols is for p-polarization, and this with symbol + is for s-polarization.

Dielectric case. Figure 10 shows the force in the Z-direction, normalized in respect to the intensity of the field at the center of the sphere, for light at an angle of incidence $\theta = 0°$. A priori, the force seems always negative, i.e., the sphere is attracted towards the surface, so in a direction opposites to the propagation direction. In fact, we see in the inset, that the force becomes positive when the sphere goes far from the surface. This complex behaviour can be explained as followed. The dipole moment associated to the sphere, induced by the incident field, radiates propagating and evanescent field. These field are reflected by the surface, hence the sphere interacts with its own evanescent field. As known, a small dielectric sphere is always attracted by the higher intensity field and so the sphere is attracted in the direction of the surface. When the sphere goes far from the surface the force due to the evanescent wave vanishes and then stays only the scattering force due to the incident field, that is why the force goes to a limit which is the radiation pressure on the sphere in free space. Notice the difference of magnitude between the negative and positive force, who denotes the strong coupling between the sphere and the surface through the evanescent wave.

Figure 11 shows the case where the lower medium is illuminated by total internal reflection : $\theta = 42° > 41.8° = \theta_c$ where θ_c is the critical angle. As shown by fig. 11 the normalized force in the Z-direction is always negative. Far from the surface only the gradient force due to the incident field acts upon the sphere, hence the sphere is attracted to the higher intensity field. As we plot the normalized force, in respect to the intensity of the incident field at the position of the sphere, the curve is horizantal far the surface involving a force decreasing as $e^{-2\gamma z}$, where γ is the component of the wave vector perpendicular to the surface. Notice that due to the interaction of the sphere with itself, via the surface, the force decreases more strongly at small distance sphere-surface.

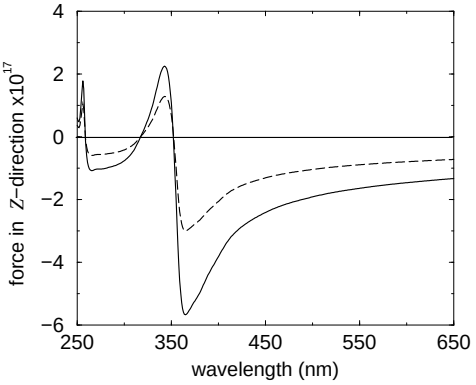

Fig. 12. – Force in the z direction for a silver sphere with an incidence angle largest than the critical angle: $\theta = 42°$. Curve in full line is for p-polarization, and in dashed line is for s-polarization.

Metallic case. In the case of metallic spheres the behaviour can be very different due to the fact that the dipole associated to the sphere is not in phase with the incident field due to the complex permittivity.[53] fig. 12 shows the case of a small sphere in silver at z_0=30nm of the surface when the ligth illuminates the surface in internal total reflexion. We see that the force in the Z-direction is also either positive or negative. In fact it depends of the phase between the dipole moment of the sphere and the applied field. When the phase is larger than $\pi/2$ the sphere is attracted towards the weaker field (for more details see Ref.[53]) Notice that the same phenomenon is used to build an atomic mirror: for frequencies of oscillation higher than the atomic frequency of resonance, the induced dipole oscillates in phase opposition with respect to the field. The atom then undergoes a force directed towards the region of weaker field. [54] The changing of sign happens when the dipole moment is in quadrature with the applied field, so when the real part of the polarizability of the sphere is null. In taking the clausius-Mossotti relation with a Drude model for the relative permittivity of the sphere, it is easy to see that this happens at the plasmon resonance and when the relative permittivity is equal to one. Between these two values the sphere is attracted towards the weaker fields.

We have not plot the case $\theta = 0°$ as the metallic case has the same behaviour of the dielectric case: when the sphere is far from the surface we have a positive force due to the scattering and absorbing force and when the sphere is closed from the surface the sphere interacts with itself for given a decreasing of the force whatever the wavelength used.

3˙3.2. Force on a large sphere.

Dielectric case. Let us now consider a sphere of radius a =100nm. In fig. 13 we present the case $\theta = 0°$. We plot the force along the Z-direction without any approximation

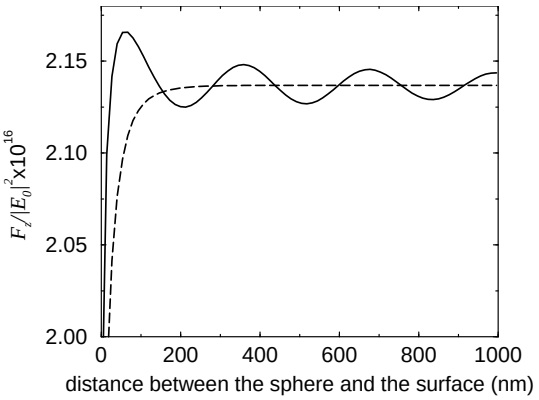

Fig. 13. – Normalized force in the Z-direction on a sphere with radius a =100nm, λ =632.8nm, and $\varepsilon = 2.25$. The light angle of incidence is $\theta = 0^\circ$. The curve in full line corresponds to the exact calculation and in dashed line with the static approximation.

(full line) and in not taking into account the retardation effect between the sphere and the surface (dashed line). The dashed line becomes constant after z=200nm, it involves that the evanescent waves are absent from the interaction process at distances beyond this limit. From the exact calculation we obtain a low force near the surface (due to the interaction through the evanescent wave as seen before) and far the surface oscillations of the force with a period $\lambda/2$. As these oscillations does not occurs in the static case, it means that they come from the multiple reflection of propagating field between the surface and the sphere. As expected, they decrease as the sphere goes far from the surface.

Figure 14 represents the case of an evanescent wave above the surface. The force in that case is always negative, as for a small sphere, but we can see that the force has oscillations as in fig. 13. We see that, conversely of a small sphere, the propagating wave becomes not negligible in the process even in an appliced evanescent field.

Metallic case. For the dielectric case, we have seen that the scattering force when the radius of the sphere increases, becomes not negligible in the computation of the force even in an evanescent field. If the sphere is metallic we must take into account, in the process, the absorbing force which produces a positive force along the Z-axis. We have not presented the study as done in fig. 14 as we have the same behaviour: oscillation of the normalized force and decrease of the force when the sphere is close from the surface. More interesting, in this case, is the transition small sphere to large sphere. In fig. 15 we plot the force along the Z-axis for a sphere in an evanescent wave versus the radius of the sphere.

When the radius is small, as the gradient force depends of a^3 and the scattering force and absorbing force of a^6, the gradient force is the most important force. Hence, the

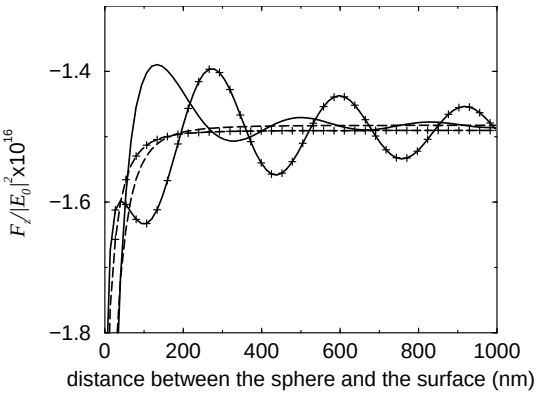

Fig. 14. – Normalized force in the Z-direction on a sphere with radius a =100nm, λ =632.8nm, and $\varepsilon = 2.25$. The light angle of incidence is $\theta = 42°$.The curves in full line correspond to the exact calculation and in dashed line to the static approximation. The curves without symbol are in p-polarization, and those with the + symbol in s-polarization.

variation of the force is cubic for small radius. The force is negative for $\lambda = 300$nm (dipole moment in phase with the applied field) and positive for $\lambda = 340$nm (dipole moment in opposition with the applied field). When the radius grows the scattering and absorbing force can not be considered negligible, as shown by the curve obtained for $\lambda = 300$nm in s-polarization. For this curve when the radius increases, the scattering

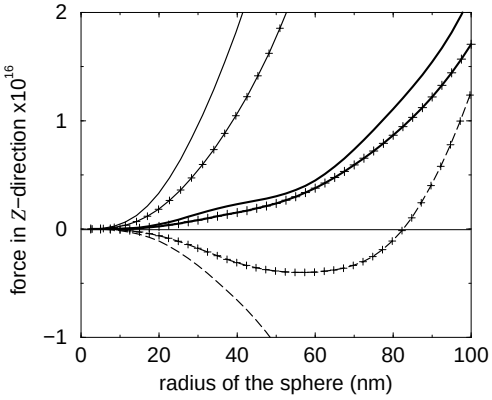

Fig. 15. – Force along the Z-direction on a silver sphere located at z_0 =100nm, with $\theta = 50°$, versus the radius a for $\lambda = 300$nm (dashed line), $\lambda = 340$nm (full line), and $\lambda = 351.5$nm (thick line). Symbol +: s-polarization; without symbol: p-polarization. The interaction between the sphere and the surface is not taken into account.

force and absorbing force become predominant and change the sign of the force imposed by the gradient force when the radius was small. This not occurs in p-polarization.[53] Note that at the plasmon resonance ($\lambda = 351.5$nm) as the dipole moment is in quadrature with the applied field, we have not a gradient force for a small sphere. Hence, we have only a very small scattering and absorbing force which increase when the radius increases.

3˙4. *Conclusion.* – This present section deals with a theoretical study of the optical forces acting upon a particle on a dielectric plane surface either illuminated at normal incidence or under total internal reflection. This study is done both with the coupled dipole method and Maxwell's stress tensor. The advantage to take the coupled dipole method is the possibility to compute in an exact form the forces for any arbitrary form for the object studied.

We observe that when the incident wave is propagating, the difference between the force acting on a dielectric sphere and that on a metallic sphere is very small: only the decreases of the force when the sphere is close to the surface is changed. The main difference between the two cases (dielectric and metallic) arises however on illumination under total internal reflection. In that case, the effect on a small silver sphere is completely different to that observed on a dielectric sphere. Depending on the wavelength, the gradient force due to the incident field can be either repulsive or attractive. The change of sign happens both at the plasmon resonance and when ε becomes close to one. In the interval between these two values the gradient force is positive.

For large sphere the presence of the multiple reflection between the sphere and the surface produces oscillation of the force in the dielectric and metallic case. But in the metallic case when the sphere becomes large the scattering and absorbing force can change an attractive force on a repulsive force in s-polarization.

* * *

This work has been supported by the Europena Union. J.R. A-G. also thanks a scholarship from Comunidad Autónoma de Madrid.

REFERENCES

[1] KLAR T., PERNER M., GROSSE S., PLESSEN G. V., SPIRKL W. and FELDMANN J., *Phys. Rev. Lett.*, **80** (1998) 4249.
[2] KRENN J. R., DEREUX A., WEEBER J. C., BOURILLOT E., LACROUTE T., GOUDONNET J. P., SCHIDER G., GOTSCHY W., LEITNER A., AUSSENEGG F. R. and GIRARD C,. *Phys. Rev. Lett.*, **82** (1999) 2590.
[3] LIU C., KAISER T., LANGE S., SCHWEIGER G., *Opt. Commun.*, **117** (1995) 521.
[4] COLLOT L., LEFÈVRE-SEGUIN V., BRUNE M., RAIMOND J. M. and HAROCHE S., *Europhys. Lett.*, **23** (1993) 327.
[5] KNIGHT J. C., DUBREUIL N., SANDOGHDAR V., HARE J., LEFÈVRE-SEGUIN V., RAIMOND J. M. and HAROCHE S., *Opt. Lett.*, **20** (1995) 1515.
[6] WEISS D. S., SANDOGHDAR S., HARE J., LEFÈVRE-SEGUIN V., RAIMOND J. M. and HAROCHE S., *Opt. Lett.*, **20** (1995) 1835.

[7] Griffel G., Arnold S., Taskent D., Serpengüzel A., Connolly J. and Morris N., *Opt. Lett.*, **21** (1996) 695.
[8] Pohl D. W. and Courjon D., *Near Field Optics*, in *Kluwer Academic Publishers*, edited by Pohl D. W. and Courjon D. (Dordrecht) 1993.
[9] Greffet J. J. and Carminatti R., *Prog. Surf. Sci.*, **56** (1997) 133.
[10] Inouye Y. and Kawata S., *Opt. Lett.*, **19** (1994) 159.
[11] Kawata S., Inouye Y. and Sugiura T., *Jpn. J. Appl. Phys.*, **33** (1994) 1725.
[12] Madrazo A. and Nieto-Vesperinas M., *J. Opt. Soc. Am. A*, **14** (1997) 2768.
[13] Gu M. and Ke P. Ch., *Opt. Lett.*, **24** (1999) 74.
[14] Antonoyiannakis M. I. and Pendry J. B., *Europhys. Lett.*, **40** (1997) 613.
[15] Burns M. A., Fournier J. M. and Golovchenco J. A., *Phys. Rev. Lett.*, **63** (1989) 1233.
[16] Bayer M., Gutbrod T., Reithmaieri J. P., Forchel A., Reinecke T. L., Knipp P. A., Dremin A. A. and Kulakovskii V. D., *Phys. Rev. Lett.*, **81** (1998) 2582.
[17] Ashkin A. and Dziedzic J. M., *Phys. Rev. Lett.*, **38** (1977) 1351.
[18] Bryant H. C. and Cox A. J., *J. Opt. Soc. Am.*, **56** (1966) 1529.
[19] Fahlen T. S. and Bryant H. C., *J. Opt. Soc. Am.*, **56** (1968) 304.
[20] Khare V. and Nussenzveig H. M., *Phys. Rev. Lett.*, **38** (1977) 1279.
[21] Owen J. F., Chang R. K. and Barber P. W., *Opt. Lett.*, **6** (1981) 540.
[22] Arias-González J. R. and Nieto-Vesperinas M., *Opt. Lett.*, **25** (2000) 782.
[23] Chylek P., Pendleton J. D. and Pinnick R. G., *Appl. Opt.*, **24** (1985) 3940.
[24] Arias-González J. R. and Nieto-Vesperinas M., submitted J. Opt. Soc. Am. A.
[25] Arias-González J. R., Nieto-Vesperinas M. and Madrazo A., *J. Opt. Soc. Am. A*, **16** (1999) 2928.
[26] wannemacher R., Pack A and Quinten M., *Appl. Phys. B*, **68** (1999) 225.
[27] Ashkin A.,*Phys. Rev. Lett.*, **24** (1970) 156.
[28] Ashkin A.,*Phys. Rev. Lett.*, **25** (1970) 1321.
[29] Ashkin. A, Dziedzic J. M., Bjorkholm J. E. and Chu S.,*Opt. Lett.*, **11** (1986) 288.
[30] Ashkin A., Dziedzic J. M. and Yamane T., *Nature*, **330** (1987) 769.
[31] Block S. M., Blair D. F. and Berg H. C.,*Nature*, **338** (1989) 514.
[32] Ashkin A.,*Proc. Natl. Acad. Sci. USA*, **94** (1997) 4853.
[33] Novotny L., Bian R. X. and Sunney Xie X.,*Phys. Rev. Lett.*, **79** (1997) 645.
[34] Tanaka M. and Tanaka K.,*J. Opt. Soc. Am. A*, **15** (1998) 101.
[35] Renn M. and Pastel R.,*J. Vac. Sci. Technol. B*, **16** (1998) 3859.
[36] Svoboda K. and Block S.,*Opt. Lett.*, **19** (1994) 930.
[37] Sugiura T., Okada T., Inouye Y., Nakamura O. and Kawata S.,*Opt. Lett.*, **22** (1997) 1663.
[38] Omori R., Kobayashi T. and Suzuki A.,*Opt. Lett.*, **22** (1997) 816.
[39] Gu M. and Ke P.,*Appl. Phys. Lett.*, **75** (1999) 175.
[40] Antonoyiannakis M. I. and Pendry J. B.,*Phys. Rev. B*, **60** (1999) 2363.
[41] Bayer M., Gutbrod T., Forchel A., Reinecke T. L., Knipp P. A., Dremin A. A., Kulakovskii V. D. and Reithmaier J. P.,*Phys. Rev. Lett.*, **81** (1997) 2582.
[42] Kawata S. and Sugiura T.,*Opt. Lett.*, **17** (1992) 772.
[43] Almaas E. and Brevik I.,*J. Opt. Soc. Am. B. B*, **12** (1995) 2429.
[44] Lester M. and Nieto-Vesperinas M.,*Opt. Lett.*, **24** (1999) 936.
[45] Visscher K. and Brakenhoff G. J.,*Optik*, **89** (1992) 174.
[46] Stratton J. A.,*Electromagnetic theory*, McGraw-Hill, New-York 1941.
[47] Barton J. P, Alexander D. R. and Scaub S. A.,*J. Appl. Phys.*, **66** (1989) 4594.
[48] Chang S., Jo J. H. and Lee S. S.,*Opt. Comm.*, **108** (1994) 133.
[49] Purcell E. M. and Pennypacker C. R.,*Astrophys. J.*, **186** (1973) 705.

[50] RAHMANI A., CHAUMET P. C., DE FORNEL F. and GIRARD C.,*Phys. Rev. A*, **56** (1997) 3245; CHAUMET P. C., RAHMANI A., DE FORNEL F. and DUFOUR J.-P,*Phys. Rev B*, **58** (1998) 2310.
[51] CHAUMET P. C. and NIETO-VESPERINAS N., in press at *Opt. Lett.*
[52] CHAUMET P. C. and NIETO-VESPERINAS N.,*Phys. Rev. B*, **61** (2000) 14119.
[53] CHAUMET P. C. and NIETO-VESPERINAS N., accepted at *Phys. Rev. B.*
[54] COGNET L., SAVALLI V., HORVATH G. Z. K., HOLLEVILLE D., MARANI R., WESTBROOK C. I., WESTBROOK N., and ASPECT A.,*Phys. Rev. Lett.*, **81** (1998) 5044;LANDRAGIN A., COURTOIS J.-Y., LABEYRIE G., VANSTEENKISTE N., WESTBROOK C. I. and ASPECT A.,*Phys. Rev. Lett.*, **77** (1996) 1464.